Polarization-driven High Rabi Frequency of Piezotronic Valley Transistors

Ruhao Liu [1], Yaming Zhang [1], Yuankai Zhou [1], Jiaheng Nie [2], Lijie Li [3*] and Yan Zhang [1,3,4*]

[1] *School of Physics, University of Electronic Science and Technology of China, Chengdu 610054, China*

[2] *School of Cybersecurity, Chengdu University of Information Technology, Chengdu 610225, China*

[3] *College of Engineering, Swansea University, Swansea, SA1 8EN, UK*

[4] *Beijing Institute of Nanoenergy and Nanosystems, Chinese Academy of Sciences, Beijing 100083, China*

*To whom correspondence should be addressed, E-mail: zhangyan@uestc.edu.cn and L.Li@swansea.ac.uk

Abstract

The properties of spin and valley transport of piezotronics valley transistor is studied based on a normal/ferromagnetic/normal (NFN) structure of monolayer (ML) transition metal dichalcogenides (TMDs). Rabi frequency reach up to 4200 MHz based on piezotronics effect, which is about 1000 times higher than that of ZnO/CdO quantum well devices. Strain-induced strong polarization can control properties of spin and valley transport in piezo-phototronic transistor. The strong polarization can be applied on the modulation of the valley qubit. The spin and valley conductance and the spin and valley polarizability are calculated theoretically. The strong polarization can be applied on the manipulation of valley qubit, which paves a new way to quantum computing applications based on piezotronic valley transistors.

Keywords: piezotronics, spintronics, valleytronics, monolayer transition metal dichalcogenides, valley qubit

1. Introduction

Piezotronics and piezo-phototronics are two promising fields with huge research prospect and application potential providing an attractive platform, which play a pivotal role for many novel devices[1, 2], such as nanogenerators[3], strain sensors[4], field-effect transistors[5], solar cells[6] and light-emitting diodes (LEDs)[6]. Piezoelectric semiconductors, such as ZnO, GaN and ML MoS_2, are used for piezotronic and piezo-phototronic materials because electronic transport and optical excitation processes can be effectively controlled by strain-induced polarized charges[7-9]. Quantum devices based piezotronic transistors also have high performance, such as piezo-phototronic intersubband terahertz devices[10], piezo-phototronic spin laser[10], quantum piezotronic tunneling transistor[11] and piezotronic spin and valley transistors[12]. Related researches have also attracted increasing interest on the widely explored two-dimensional (2D) materials like TMDs[13-15].

The degree of freedom of electrons plays key roles in many research areas of modern science and technology[16]. TMDs, for their characteristics of hosting an easily accessible electronic degree of freedom, allowing for dynamic control, have been extensively studied since the landmark achievement of graphene[17, 18]. Besides the two well-known quantum degrees of freedom of electrons charge and spin, valley degree of freedom, referring to the multiple degenerate energy in the local minimum of conduction or local maximum of valence bands the electrons occupy, has also received a lot of attention[19, 20]. ML TMDs are atomically thin semiconductors with a direct band gap at two valleys in the first Brillouin zone, combined with the lack of inversion symmetry, making them the ideal materials for the study of valley[21, 22]. Due to the coupling of heavy spin orbits, the spin regulation in ML TMDs is promising and has been extensively explored and used in quantum devices[23].

Qubit plays an important role in quantum computing and quantum information processing[24, 25]. In addition to the great progress made in spin qubit, a series of theoretical and experimental breakthroughs have been made in the study of valley qubit[26, 27]. Recently, some studies have shown that the manipulation of the valley qubit can be realized by applying a gate voltage creating confinement to MoS_2 nanosheets[28]. Some research have shown that both spin and valley qubit can be manipulated[29]. Rabi frequency is a key performance index for estimating the speed of spin and valley qubits manipulation in devices[30]. It was reported

that strain induced polarization of the quantum well adjusts the spin-orbit interaction coefficient, thereby increasing the Rabi frequency by a factor of 20, which is of great significance for the study of spin qubit[12].

Recent studies have shown that the spin and valley polarization can be obtained in a NFN junction based on 2D materials through the combined methods of applying a magnetic field as well as an electric field induced by a gate voltage[31]. Current research show that electric field intensity is one of the essential conditions for the control of spin and valley degree of freedom[32, 33]. Piezoelectric field formed by polarization of positive and negative charges under strain is an ideal choice. It has been proved that a strong electric field can be generated at the piezoelectric charge interface[34, 35]. Recent study showed that the strong piezoelectric electric field generated by strain can reach to the level of MV/cm at the interface of ML MoS_2, showing a good strain-regulated spin and valley characteristics[12]. It has also been proved that spin qubits can be manipulated by the stress-induced polarization field in a ZnO/CdO quantum well[36]. However, up to now, there is a lack of systematic theoretical research on the properties of strong piezoelectric fields in two-dimensional materials and related device design, and the manipulation of valley qubit by piezoelectric fields still remains unexplored, especially for 2D TMDs with broken inverse symmetry.

In this paper, we propose the NFN structures that regulate spin and valley by strong piezoelectric polarization field. We apply ferromagnetic material EuO in the middle of the NFN structure to magnetize the ML TMDs[37, 38]. We systematically investigate the piezopotential and piezoelectric field of MoS_2, $MoSe_2$, $MoTe_2$, WS_2, WSe_2 and WTe_2 and explore the effect of piezoelectric field and deformation potential on the band structure and electron transport characteristics of TMDs. It is found that the piezoelectric field has a dominant influence on the spin and valley transport and polarization characteristics, in this way, the influence of the piezoelectric field on the transport characteristics of ML TMDs is emphatically discussed. Under the condition of applying strain along both sides of the X-axis, the transportation of spin and valley can be controlled and different transport results are shown in different TMDs. It is well known that the electrical field in two dimensional materials is very common to reach 10 MV/cm experimentally by gate way[39]. The electric field reach up to 3 MV/cm, which is calculated by $D = \varepsilon^{hBN}(V_B/h_B - V_T/h_T)/2$ in this paper. According to the expanded Maxwell's

equations based on polarization coined by Zhong Lin Wang[40], the displacement field include the contribution of external electric field (gate field in this case) and polarization induced by piezoelectric or triboelectric. The electric field by the polarization act as important role in TMD. We explored the piezoelectric field of ML TMDs under strain regulation, and found that a strong piezoelectric field of 1 MV/cm can be achieved at the ferromagnetic interface in ML TMDs based on the NFN structure. We calculated the electronic density of states based on ML MoS_2. It shows the polarization field plays a good confinement characteristic for valley in the device. We found that the intervalley coupling index can be modulated by a piezoelectric electric field induced by periodically varying strains and the Rabi frequency can be further regulated. The results show that Rabi frequency increases from 385 MHz to 4200 MHz by applying strain, increased by 11 times, which shows an excellent effect of strain on the modulation of the valley qubit. We compare the regulation effect of piezoelectric field and deformation potential, and mainly analyze the influence of piezoelectric field on spin and valley transport of ML TMDs, show the valley and spin polarization properties of different TMDs materials, and the ideal polarized regions. This study provides a complete theoretical guidance for exploring piezoelectric regulation of spin and valley transport and the application of quantum piezotronics in the field of quantum computing is expanded.

2. Model of Piezotronic Effect on Spin and Valley Transport

In order to systematically illustrate the regulating effect of strong piezoelectric polarization field on valley and spin, we explore the NFN structures based on ML TMDs. We take ML MoS_2 as an example. Fig. 1(a) is a schematic diagram of the NFN structure. The left and right are source and drain electrodes respectively, the middle is ferromagnetic region, and the bottom is the flexible substrate. When tensile or compressive strain is applied laterally, the positive and negative charge symmetry centers of ML MoS_2 on the substrate will change, as shown in Fig. 1(b). For example, when the applied strain is 3%, the negative charge in the ferromagnetic region is distributed at the left interface and the positive charge is distributed at the right interface, resulting in an approximately one-dimensional field[41]. In this way, we can obtain the piezoelectric polarization field along the horizontal direction, and the corresponding electric field intensity can be calculated as shown in Fig. 1(c). At 3% strain, a strong electric field of

more than 1 MV/cm can be achieved at the interface of MoS_2. The MoS_2 is used in this example, and other TMD materials will have similar behaviors. The values of piezopotential and piezoelectric field intensity corresponding to MoS_2, $MoSe_2$, $MoTe_2$, WS_2, WSe_2 and WTe_2 are listed in Table 1, where U represents piezopotential and E represents piezoelectric field, as shown in Table 1, MoS_2, $MoSe_2$ and $MoTe_2$ all show piezopotential and high piezoelectric field and better polarization characteristics in the electron transport analysis in terms of spin and valley properties. In all the above cases, the magnitude of the strain was set to 3%.

For the NFN structure, the spin- and valley-dependent quantum transport properties can be obtained from the time-dependent Schrödinger equation

$$i\hbar\frac{\partial}{\partial t}\psi = H\psi \tag{1}$$

where, H represents a Hamiltonian, ψ is wave function and E is an eigenvalue and $\hbar$ is the reduced Planck constant. The transport properties of the two structure can be described by discretizing the system into a series of transverse strips along the transport direction[42]. The transmission conductivity and electron density distribution are obtained by solving the Schrodinger equation under special boundary conditions.

By fitting to first-principles band structure calculations, the parameters of Hamiltonian can be obtained for the four group-VI dichalcogenides[22]

$$H = v\left(\tau_z k_x\sigma_x + k_y\sigma_y\right) + \frac{\Delta}{2}\sigma_z - \lambda_v\tau_z\frac{\sigma_z - 1}{2}s_z \tag{2}$$

The first and second term denote the band Hamiltonian without the spin-orbit coupling where τ_z =±1 denotes the valleys index (1 for K valley and -1 for K' valley), v is the Fermi velocity and Δ is the parameter for energy gap. σ_x, σ_y, σ_z are the Pauli matrices. k_x and k_y are the wave vector momentum. The third term on the right side of equation (2) represents the spin-orbit coupling, it is represented by a product of the spin angular momentum and the orbital angular momentum, λ_v is the coupling constant which stands for spin splitting energy of the valence band.

As we expand the time-dependent wavefunction $\psi(t)$ into the complete set of eigen-

functions Φ_n of H_0:

$$\dot{C}_p(t) = -\frac{i}{\hbar}\sum_n V_{pn}(t)\exp(-iE_{np}t/\hbar)C_n(t) \tag{3}$$

where $E_{np} \equiv E_n - E_p$ and $V_{pn}(t) = \langle \phi_p | V(t) | \phi_n \rangle$. For simplicity, the cases at $V_{nn} = 0$ for all n. According to[43], if the laser field is modelled as a harmonic perturbation at some frequency ω_L:

$$V(t) = V_0 \cos \omega_L t \tag{4}$$

The "Rabi frequency" is given by

$$\Omega_R \equiv \left[\Delta^2 + V_0^{\,2}/\hbar^2\right]^{1/2} \tag{5}$$

where $\Delta = (\omega_0 - \omega_L)$. The intervalley coupling constant is a perturbation term in the laser field[43]. According to previous works, Rabi frequency can be electrically modulated using gate voltage[44]. Moreover, it has been investigated in experiment that the modulation of the Rabi frequency can be realized via electric fields, and the resonance frequency dependence on gate voltage is nearly linear[45]. According to previous theoretical[43, 46] and experimental[44, 45] studies, it is possible to use an oscillating piezoelectric field generated by strain as perturbation term V_0, which is the key parameter " Λ " generated by piezoelectric field. According to[28], the perturbation term V_0 is generated by applying oscillating voltages $V = V_1 + V_2\left[\cos(\omega t) - 1\right]$. Strain can generate the same electric field, Rabi frequency up to 4200 MHz can be reached theoretically. In experiment, Rabi frequency reaches 2006 MHz by gate voltage[45].

In the NFN structure, the term $H_z = s_z h$ describes the proximity exchange coupling at the interface between the TMD and the ferromagnetic insulator. The proximity exchange coupling Hamiltonian contains Zeeman-like exchange coupling[47]. When ML TMDs are placed on a ferromagnetic substrate, the magnetic exchange potential penetrates the atomic layer, causing Zeeman-type spin splitting related to the magnetic moment of the substrate [48]. s_z=±1 represents the electron spin up and spin down, h is the exchange field existing in the ferromagnetic region. In our calculation, the second-order terms of spin-orbit coupling

associated with the spin splitting in the conduction band $\lambda_c \tau_z \frac{\sigma_z + 1}{2} s_z$ is taken into consideration[23], where the coupling is attributed to mixing with high-energy atomic orbitals. λ_c is another coupling constant which represents the spin splitting energy of the valence band, and the coupling is attributed to mixing with high-energy atomic orbitals. In most situations, coupling constant λ_c is smaller than λ_v [49]. When there is a piezoelectric field, it mainly affects the onsite term in the Hamiltonian[50], under this condition, the whole Hamiltonian of our model is given as:

$$H = v\left(\tau_z k_x \sigma_x + k_y \sigma_y\right) + \frac{\Delta}{2}\sigma_z - \lambda_v \tau_z \frac{\sigma_z - 1}{2} s_z - \lambda_c \tau_z \frac{\sigma_z + 1}{2} s_z - s_z h + U \tag{6}$$

When a uniform strain is applied on the NFN structure of ML TMDs, large piezoelectric field generated by strain-induced piezoelectric charges can be obtained. Approximately, it can be considered as a one-dimensional field[41]. The piezopotential in NFN junction is written as [51]:

$$U_{piezo} = \begin{cases} \frac{e_{11} s_{11}}{2\pi\varepsilon_r \varepsilon_0} \ln|x| + U_1, -d < x \le 0 \\ \frac{e_{11} s_{11}}{2\pi\varepsilon_r \varepsilon_0} \ln\left|\frac{x}{d - x}\right|, 0 < x \le d \\ \frac{e_{11} s_{11}}{2\pi\varepsilon_r \varepsilon_0} \ln|x - d| + U_2, d \le x < 2d \end{cases} \tag{7}$$

where e_{11} is the piezoelectric coefficient, s_{11} is the applied strain, ε_r is relative dielectric constant, ε_0 is vacuum permittivity, x and y are the distance away from the boundary. d is the width of the ferromagnetic region. In order to ensure that the electric potentials are equal at different regional interfaces and the logarithmic function is meaningful, we set the corresponding parameters represented by constants U_1 and U_2 respectively. An inhomogeneous potential will be generated by applying mechanical strain on both sides of the structure, as is depicted in the Fig. 1(c). The coefficients of MoS_2, $MoSe_2$, $MoTe_2$, WS_2, WSe_2 and WTe_2 used in the calculation, including Fermi velocity v, the energy gap Δ, the coupling constant λ_v and λ_c, the relative dielectric constant ε_r, the Piezoelectric Coefficients e_{11} are listed in Table 2. Due to the lack of WTe_2-related λ_c, and the large value of λ_v, we ignored this item in the calculation of WTe_2.

When there is a piezopotential U, the Rabi frequency can be greatly increased under the modulation of a dynamic piezoelectric field induced by strain, and the conductance of TMDs

in our device varies significantly with *U*, enabling good filtering[44-46]. A strong piezoelectric polarization at the NFN interface is crucial for increasing Rabi frequency[52] and valley filtering[53]. Valley states represent a degree of freedom in addition to spin and charge, characterizing and controlling valley states is critical for the encoding and read-out of valley qubits[54]. High Rabi frequency plays a significant role in the qubits[55]. Piezoelectric polarization field can control valley states and increase the Rabi frequency, which are critical to improving the valley qubit performance.

3. Results and Discussion

KWANT is a widely used numerical quantum transport calculations, and it is based on the wave function method. In this paper, we use the quantum transport package KWANT to compute the transport properties. This method is mathematically parallel to the commonly used nonequilibrium Green's function[56]. For the NFN structure, we assume that the ferromagnetic region is 20 nm[12, 57]. The infinite interfacial values of U_piezo and E_piezo in Fig. 1 are due to artificial abrupt changes at the interfaces in the electronic structures. The real interfacial values must be finite. Previous experiments reported the nonlinear Hall effect in electrical transport in bilayers of the non-magnetic quantum material WTe_2 under time-reversal-symmetric conditions. It found that the electric field can reach up to 3 MV/cm[39]. Thus, the minimum piezo-charge width is 0.05 nm. In this manuscript, we choose 0.2 nm as the width of piezo-charge with the corresponding electric field of 1 MV/cm. According to[58], there is no flux through the flat face inside the line charge thus the electric field is zero, the electric field is $E = \frac{\lambda}{2\pi\varepsilon_0 a}$ where λ is charge density per unit length, and *a* is the distance from external point to wire. The electric potential is given by: $U = \int_{P_0}^{P} \vec{E} d\vec{l} = \frac{\lambda}{2\pi\varepsilon_0} \ln \frac{r}{r_0}$. For MoS_2, the U_piezo and E_piezo are 0.15 V and 1 MV/cm, respectively. The width of piezo-charge distribution is 0.2 nm. The calculation results are consistent with the experiments[59, 60].

Taking ML MoS_2 as an example, an energy diagram at the K and K′ valleys showing the energy splitting of the bands in each region of the NFN junction are shown in Fig. 2. For normal region without strain, as shown in Fig. 2(a), there is a small spin splitting exists in the

conduction band at K and K′ valley, which is demonstrated in previous works[61, 62]. The conduction-band spin splitting is valley dependent due to the time-reversal symmetry and leads to weak valley-spin coupling, and it is induced by small contributions from *Mo-dxz*, *dyz*, and *S-px*, *py* orbitals[62]. Compare with the conduction band, the valence band in the normal region has larger spin splitting at K and K′ valley, which is induced by the interactions in the heavy Mo atoms[62]. The valence bands of two valleys show opposite spin splitting, the two valleys in valence bands correspond to nearly the same energy. Indicating that the K↑ is degenerate with the K′↓ while the K↓ is degenerate with the K′↑[62-64]. In the presence of exchange field, as shown in Fig 2(d), the spin-up and spin-down bands at K and K′ valley are separated by the exchange field induced Zeeman splitting[65], the lifting degeneracy is observed in the K↑ and K′↓ as well as the K↓ and K′↑[47]. It has been demonstrated that the energy shift in each valley can be of the order of 0.01 eV in single layer WS_2 using circularly polarized light[66]. Higher energy splitting of 0.069 eV in graphene also has been observed by applying circularly polarized light[67]. In ferromagnetic region, the band gaps of K′↑ and K′↓ widen while those of K↑ and K↓ narrow[38, 47].

Due to the existence of a ferromagnetic exchange field, the spin-up bands move downward while the spin-down bands move upward, in this way, the spin splitting in K′ valley is larger than that in the normal region while spin splitting in K valley is smaller than that in the normal region. The opposite situation will happen when there is an antiferromagnetic exchange field. [38, 65]. The results indicate that the exchange field can further amplify the difference between the spin-splitting gaps at the two valleys, which is important to the valley-polarized transport. When the strain is 3% and the effect of piezoelectric field is considered, as shown in Fig. 2(b) and (e), compared with strain=0, further spin splitting spin at K and K′ valley is small, and the band is shifted downward by 0.17 eV. When the strain is 3%, the effect of deformation potential is considered, the conduction band minimum moves downward by 0.14 eV, the valence band maximum moves upward by 0.16 eV, and the band gap decreases by 0.3 eV, as shown in Fig.2 (c) and (f). The effects of the exchange field, deformation potential and piezoelectric field on the energy band are analyzed. The exchange field lifts the degeneracy of spin and valley, the piezoelectric field causes the band translation and the deformation potential can reduce the band gap.

NFN structure usually have a unified band structure in previous works[68, 69]. When there is a magnetic field or a potential barrier exists in the middle region of the device[32, 70, 71], the band structures of N and F can be calculated separately due to the spin splitting in F regions. In these models, the proximity exchange coupling $H_z = s_z h$ are added in F regions[47]. Due to the ferromagnetic proximity effect, the spin-up and spin-down bands at K valley and K′ valley are separated by the exchange field[65, 69].

KWANT, an open-source Python package[72], is used in our simulation. The experiments[73] found supercurrent rectification and magnetochiral effects in symmetric Josephson junctions, KWANT provides a semiquantitative description of experimental data. KWANT has been applied to quantum transport in the NFN structure [74], nonlocal spin valves based on a nanoribbon[75]. We use KWANT to calculate the band structure in NFN structure, the Hamiltonian of the N region and the F region are different, the normal and ferromagnetic regions exhibit different band structures.

Previous experiments[76] founded normal and ferromagnetic regions exhibit different band structures. The band structures of N and F are calculated in the whole device. The superposition model of Hamiltonian can be linear[77], based on the $k \cdot p$ theory[78] and the tight-binding model[32, 79]. DFT also exhibits better calculation accuracy[80].

Fig. 3 shows the density distribution of electrons in NFN structure of ML MoS_2 with Fermi level fixed at -1.05 eV. Under the strain of -0.5%, the electrons of K and K′ valley are bound to the right and left side respectively. It shows a strong confinement under strain regulation. At strain of -0.5%, the up-spin electrons in K valley is mainly reside in the right normal region, as shown in Fig. 3(a). Under strain of -0.2%, and the up-spin electrons in K′ valley mainly occupy the normal area on the left, as shown in Fig. 3(b). The electrons from different valley are confined in the different sides of the device with compressive strain, this phenomenon shows that electrons of the different valley degree of freedom have good confinement effect under different strains. The result shows the ability to confine quantum dot and manipulate electron degrees of freedom and provides the possibility for the piezoelectric polarization field to control valley qubit.

The ribbon structure seems difficult to get required confined states for spin and valley. However, under suitable conditions, the ribbon structure can confine the spin and the valley.

According to[81], the device based on a ribbon of graphene is proposed. The ribbon region between the two potential barriers with a length of L and a width of W can be assumed to be a dot. And the width of a quantum-dot is about 30 nm. In this study, Fig. 3 has shown the density states distribution under the piezoelectric polarization field. The states for spin and valley can be confined to quantum dots, and the width of the quantum dots is about 20 nm. The results are consistent with previous research work[82].

Pure valley qubits realized in MoS_2 are known to be challenge by large magnetic fields due to strong intrinsic spin-orbit coupling in conduction band[83]. According to[83], combining spin-valley (Kramers) qubit at low magnetic fields appears to be the most realistic option to overcome the challenge. Based on this point of view, we reduced the magnetic field parameter in the calculation to 30 meV, which is corresponding to 7.7 T[84]. Under this condition, as Figure S2 shows, spin and valley polarization can be accessed by strain. The spin and valley polarization we obtained mainly owing to the splitting of the valence bands[85, 86]. According to[83], the realization of pure valley qubits in MoS_2 requires a large magnetic field. In this study, the exchange field is 100 meV, which are in a similar range for the previous studies[31, 65]. According to[84], the equivalent magnetic field is about 25.6 T, which is a relatively large magnetic field. The magnetic field in the experiment attained over 60 T[87]. Therefore, although in the initial calculation, we did not combine spin-valley qubit at low magnetic fields[83], the pure spin and pure valley qubits can be obtained in the structure we proposed because of the larger magnetic field.

Rabi frequency, as an effective parameter to describe the performance of valley qubit, is also calculated in the NFN structure based on ML MoS_2. It is demonstrated that the gate voltage with frequency can change the strength of the intervalley coupling Λ [28]. A combination of fixed strain and dynamic strain is used to adjust Λ. The confinement piezopotential is now modulated by applying oscillating strain and can be defined as $s = s_1 + s_2\left[\cos(\omega t) - 1\right]$. s_1 is fixed at 5% while $s_2\left[\cos(\omega t) - 1\right]$ is a quantity that changes over time, $s_1 = 1\%$ is the amplitude and ω is the frequency. Thus, a periodically varying piezoelectric field of 1.5-2 MV/cm can be generated. According to ref[28], the value of Λ can be adjusted, ranging from

0.008eV to 0.088eV. Rabi frequency $\Omega = \sqrt{(\omega - \omega_0)^2 + (\Lambda/\hbar)^2}$ weakly depends on the driving oscillation frequency (ω_0 is the resonant frequency), while it mainly depends on the intervalley coupling Λ and can be adjusted from 385 MHz to 4200 MHz. It shows that the NFN device based on strain regulation can not only be applied to valley qubit, but also can greatly improve the performance of valley qubit.

The Rabi frequency is a quantity that characterizes the interaction between two-level quantum systems and external electromagnetic fields. It describes the rate at which a quantum system transitions between its two energy levels under the influence of an oscillating field. Therefore, a device with a higher Rabi frequency has a greater usefulness in qubit applications. The Rabi frequency in this TMD can reach up to 4200 MHz theoretically, which is much higher than that in carbon nanotubes[26, 88], as shown in Table 3. As for graphene, the Rabi frequency can reach up to 100 GHz[89]. Graphene-based valley qubits is very interesting and has made great progress in theory[81] and experiment[90-92]. However, compared to other 2D material systems like graphene and carbon nanotube, TMDs offer some advantages for qubit implementations. TMDs exhibit long spin lifetimes and valley coherence times[93]. TMDs also allow fast spin rotation, which is ideal for qubit operations[94]. Furthermore, TMDs have a stronger binding energy, indicating a higher stability over time, which is necessary for realizing practical quantum devices[95].

TMDs with suitable band gap offer some advantages for qubit implementations, including long spin lifetimes and valley coherence times[93], fast spin rotation[94], as well as stronger binding energy[95]. It estimated that the electrically driven qubit Rabi frequencies of the order of 10-100 MHz in MoS_2[96]. R. J. Schoelkopf et al. proposed a realizable architecture using one-dimensional transmission line resonators, and the vacuum Rabi frequency reaches up to 220 MHz[97]. Brooks Matthew et al. showed the Rabi oscillations up to 250 MHz by a combination of a sufficiently small quantum dot radius and a large perpendicular magnetic field[98]. The Rabi frequency in our structure can reach up to 4200 MHz theoretically, which is higher than that of electrically driven qubit. In graphene, the Rabi frequency can be 100 GHz[89]. Although the 4200 MHz is not higher than graphene according to theoretical calculations, third-generation semiconductors are considered as good candidate for qubits due

to wide bandgap and piezotronic effect[36], and high spin-orbit interaction induced by the polarization in ZnO/CdO QWs quantum piezotronic devices increase the Rabi frequency from 0.19 MHz to 4.05 MHz by piezotronic effect.

The Rabi frequency of different TMDs such as MoS_2, $MoSe_2$, $MoTe_2$, WS_2, WSe_2 and WTe_2 are studied. In excitonic model of the optical Stark effect of monolayer WS_2, a Rabi frequency of 750 MHz is achieved[99]. A light-induced spin Hall effect for interlayer exciton gas in monolayer van der Waals heterostructure is studied and the calculated Rabi frequency of $MoSe_2$ and WSe_2 is 229 MHz[100]. The electrically driven MoS_2 qubit Rabi frequencies of the order of 100 MHz can be achieved[96]. It is reported that a Rabi frequency of 33 MHz is attained in WTe_2[101]. The Rabi frequency of $MoTe_2$ is rarely reported, the 1H-$MoTe_2$ possess tunable band structures (0.88-1.1 eV) controlled by thickness and has strong spin-orbit coupling[102]. Based on the comparison of Rabi frequency of different TMDs, Rabi frequency of WS_2 reach up to 750 MHz.

Fig.4 systematically shows the effects on electron transport in ML MoS_2 considering the piezoelectric field (shown in the first row), the deformation potential (shown in the second row), and both (shown in the third row). The strain varies from -6% to 6%, the Fermi level is set from -1.25 eV to -0.75 eV. When piezoelectric field is taken into consideration, the distribution of conductivity varies according to different valleys and spins, as shown in Fig. 4(a-d). The K↑electrons display a high conductance when Fermi level is fixed from -1.1 eV to -0.86 eV and strain is set from -2.5% to 1%. The K↓ electrons show a high conductance when Fermi level is fixed from -1.13 eV to -0.88 eV and strain is set from -1% to 2.2%. As for K′↑electrons, the conductance region mainly occupies the bottom left of parameter plane, where Fermi energy is from -1.22 eV to -0.98 eV and strain is from -2.2% to 1%. As for K′↓ electrons, the conductance region is concentrated on the upper right of parameter plane, where Fermi energy is from -1 eV to -0.75 eV and strain is from -1.2% to 2.6%. Fig. 4(e-h) show the distribution of conductivity when deformation potential is considered only. Under the condition that only the influence of deformation potential is considered, the band gap decreases with the increase of strain[103], and the conductance is improved. However, the influence of strain on electron spin and valley is not reflected under this condition, and the four degrees of freedom are mainly shifted up and down in the figure by the change of Fermi level. Fig. 4(i-l) show the conductance distribution

with the effects of piezoelectric field and deformation potential. The conductance of the third row is higher than that of the first row, but the conductance distribution is basically the same, indicating that the piezoelectric field rather than the deformation potential is the main factor affecting the electron spin and valley distribution. The piezoelectric field still maintains dominance as the stress increases to ±6%, which is piezotronics effect.

Fig. 5 shows the spin-polarized ratio P_s of ML TMDs based on the NFN structure as a function of strain and Fermi level. "1" stands for full spin up polarization, and "-1" means full spin down polarization. For MoS_2, $MoSe_2$ and $MoTe_2$, when the Fermi level ranges from -1.1 eV to -0.9 eV, -1.0 eV to -0.75 eV, and -0.85 eV to -0.55 eV, respectively, nearly complete spin upward polarization is observed under compressive strain, while under tensile strain, it exhibits nearly complete spin downward polarization, as shown in Fig. 5(a-c), reflecting the excellent selective behavior of strain for spin. In WS_2, when Fermi level is distributed between -1.05 eV and -0.8 eV, and the absolute value of strain is greater than 1%, the down-spin polarization generated by tensile strain and the up-spin polarization generated by compressive strain is appeared simultaneously, as shown in Fig. 5(d). Similarly, in WSe_2 and WTe_2, within the Fermi levels of -0.9 eV to -0.75 eV, -1.25 eV to -1.1 eV (for WSe_2, as shown in Fig. 5(e)), -0.8 eV to -0.55 eV, and -1.0 eV to 0.93 eV (for WTe_2, as shown in Fig. 5(f)), under the influence of at relatively large tensile and compressive strain, approximately complete down-spin and up-spin polarization will be generated, respectively.

Fig. 6 shows the valley-polarized ratio P_v of ML TMDs based on the NFN structure as a function of strain and Fermi level. "1" stands for full K valley polarization, and "-1" means full K′ valley polarization. There are two K′ polarization regions and one K polarization region in ML TMDs, and each material has an ideal strain adjustment interval. Take MoS_2 as an example, when Fermi level ranges from -1.1 eV to -1.02 eV, under tensile strain, almost complete K valley polarization will appear, while under compressive strain, almost complete K′ valley polarization will appear. And as Fermi level changes from -0.95 eV to -0.85 eV, the situation is contrary to the former. Under tensile strain, nearly 100% K′ valley polarization will appear, while under compressive strain, nearly 100% K valley polarization will appear, as shown in Fig. 6(a). The corresponding strain regulated valley polarization regions can also be found in $MoSe_2$, $MoTe_2$, WS_2, WSe_2 and WTe_2, as shown in Fig. 6(b-f). The results indicate the effectively

modulation of valley polarization by strain.

The spin and valley polarization properties of different TMDs are studied. In Fig. 5, the spin polarization regions of MoS_2, $MoSe_2$ and $MoTe_2$ are wider than that of WS_2, WSe_2 and WTe_2. In Fig. 6, polarization regions of valley are shown in MoS_2, $MoSe_2$ and $MoTe_2$. Based on the above comparison of spin and valley polarization properties of different TMDs, MoS_2, $MoSe_2$ and $MoTe_2$ are good candidates.

4. Summary

In this study, valley and spin transport properties under the impact of stress-induced piezoelectric field and deformation potential of ML TMDs in the NFN structure have been systematically studied. We found that the NFN structure based on the strong piezoelectric field regulation has good confinement properties and can substantially adjust Rabi frequency, and can be used to regulate the valley qubit effectively. We also find that the piezoelectric field plays a dominant role in the electron transport characteristics, and further give the spin and valley polarization regions of different TMDs under the change of strain and Fermi level.. This study provides theoretical guidance for novel quantum piezoelectric devices and opens an avenue for the manipulation of valley qubit.

Acknowledgments

The authors are thankful for the support from Major Project of National Natural Science Foundation of China (Grant No. 52192612, 52192610). The authors are thankful for the support from University of Electronic Science and Technology of China (grant no. ZYGX2021YGCX001).

Reference

1. Wang, Z.L., W. Wu, and C. Falconi, Piezotronics and piezo-phototronics with third-generation semiconductors. Mrs Bulletin, 2018. **43**(12): p. 922-927.
2. Wu, W. and Z.L. Wang, Piezotronics and piezo-phototronics for adaptive electronics and optoelectronics. Nature Reviews Materials, 2016. **1**(7).
3. Wang, Z.L. and J.H. Song, Piezoelectric nanogenerators based on zinc oxide nanowire arrays. Science, 2006. **312**(5771): p. 242-246.
4. Zhou, J., et al., Flexible piezotronic strain sensor. Nano Letters, 2008. **8**(9): p. 3035-3040.
5. Wang, X., et al., Piezoelectric field effect transistor and nanoforce sensor based on a single ZnO nanowire. Nano Letters, 2006. **6**(12): p. 2768-2772.
6. Yang, Q., et al., Enhancing light emission of ZnO microwire-based diodes by piezo-phototronic effect. Nano Lett, 2011. **11**(9): p. 4012-7.
7. Zhang, Y., Y. Liu, and Z.L. Wang, Fundamental Theory of Piezotronics. Advanced Materials, 2011. **23**(27): p. 3004-3013.
8. Zhang, Y., et al., Theory of piezotronics and piezo-phototronics. Mrs Bulletin, 2018. **43**(12): p. 928-935.
9. Liu, Y., et al., Piezotronics and piezo-phototronics in two-dimensional materials. Mrs Bulletin, 2018. **43**(12): p. 959-964.
10. Xie, C., et al., Piezo-phototronic spin laser based on wurtzite quantum wells. Nano Energy, 2022. **96**.
11. Dan, M., et al., High performance quantum piezotronic tunneling transistor based on edge states of MoS2 nanoribbon. Nano Energy, 2022. **98**.
12. Liu, R., et al., Piezotronic spin and valley transistors based on monolayer MoS2. Nano Energy, 2020. **72**.
13. Fiori, G., et al., Electronics based on two-dimensional materials. Nature Nanotechnology, 2014. **9**(10): p. 768-779.
14. Xu, M., et al., Graphene-Like Two-Dimensional Materials. Chemical Reviews, 2013. **113**(5): p. 3766-3798.
15. Lin, P., C. Pan, and Z.L. Wang, Two-dimensional nanomaterials for novel piezotronics and piezophototronics. Materials Today Nano, 2018. **4**: p. 17-31.
16. Jiang, X., et al., Real-time GW-BSE investigations on spin-valley exciton dynamics in monolayer transition metal dichalcogenide. Science Advances, 2021. **7**(10).
17. Wang, Q.H., et al., Electronics and optoelectronics of two-dimensional transition metal dichalcogenides. Nat Nanotechnol, 2012. **7**(11): p. 699-712.
18. Novoselov, K.S., et al., Electric Field Effect in Atomically Thin Carbon Films. Science, 2004. **306**(5696): p. 666-669.
19. Mak, K.F., D. Xiao, and J. Shan, Light–valley interactions in 2D semiconductors. Nature Photonics, 2018. **12**(8): p. 451-460.
20. Schaibley, J.R., et al., Valleytronics in 2D materials. Nature Reviews Materials, 2016. **1**(11).
21. Liu, Y., et al., Valleytronics in transition metal dichalcogenides materials. Nano Research, 2019. **12**(11): p. 2695-2711.
22. Xiao, D., et al., Coupled spin and valley physics in monolayers of MoS2 and other group-VI dichalcogenides. Phys Rev Lett, 2012. **108**(19): p. 196802.
23. Habe, T. and M. Koshino, Anomalous Hall effect in 2H-phase MX2 transition-metal dichalcogenide

monolayers on ferromagnetic substrates (M = Mo, W, and X = S, Se, Te). Physical Review B, 2017. **96**(8): p. 085411.
24. Loss, D. and D.P. DiVincenzo, Quantum computation with quantum dots. Physical Review A, 1998. **57**(1): p. 120.
25. Imamog, A., et al., Quantum information processing using quantum dot spins and cavity QED. Physical review letters, 1999. **83**(20): p. 4204.
26. Laird, E.A., F. Pei, and L.P. Kouwenhoven, A valley–spin qubit in a carbon nanotube. Nature nanotechnology, 2013. **8**(8): p. 565-568.
27. Penthorn, N.E., et al., Two-axis quantum control of a fast valley qubit in silicon. npj Quantum Information, 2019. **5**(1): p. 1-6.
28. Pawłowski, J., D. Żebrowski, and S. Bednarek, Valley qubit in a gated MoS 2 monolayer quantum dot. Physical Review B, 2018. **97**(15): p. 155412.
29. Eich, M., et al., Spin and valley states in gate-defined bilayer graphene quantum dots. Physical Review X, 2018. **8**(3): p. 031023.
30. Nowack, K.C., et al., Coherent control of a single electron spin with electric fields. Science, 2007. **318**(5855): p. 1430-1433.
31. Li, H., et al., Gate-voltage-controlled spin and valley polarization transport in a normal/ferromagnetic/normal MoS(2) junction. ACS Appl Mater Interfaces, 2014. **6**(3): p. 1759-64.
32. Yokoyama, T., Controllable valley and spin transport in ferromagnetic silicene junctions. Physical Review B, 2013. **87**(24).
33. Tao, L.L., A. Naeemi, and E.Y. Tsymbal, Valley-Spin Logic Gates. Physical Review Applied, 2020. **13**(5).
34. Miao, M., et al., Polarization-driven topological insulator transition in a GaN/InN/GaN quantum well. Physical review letters, 2012. **109**(18): p. 186803.
35. Zhang, D., et al., Interface-induced topological insulator transition in GaAs/Ge/GaAs quantum wells. Physical review letters, 2013. **111**(15): p. 156402.
36. Fu, M., et al., Polarization-induced ultrahigh Rashba spin-orbit interaction in ZnO/CdO quantum well. Nano Energy, 2021. **88**: p. 106310.
37. Haugen, H., D. Huertas-Hernando, and A. Brataas, Spin transport in proximity-induced ferromagnetic graphene. Physical Review B, 2008. **77**(11).
38. Liu, B., et al., Simultaneous perfect polarization of spin and valley using monolayer MoS2 modulated by light and spin Zeeman field. Journal of Physics D: Applied Physics, 2021. **54**(42).
39. Ma, Q., et al., Observation of the nonlinear Hall effect under time-reversal-symmetric conditions. Nature, 2019. **565**(7739): p. 337-342.
40. Wang, Z.L., On the expanded Maxwell's equations for moving charged media system–General theory, mathematical solutions and applications in TENG. Materials Today, 2022. **52**: p. 348-363.
41. Zhang, J., et al., Band alignment of two-dimensional lateral heterostructures. 2D Materials, 2016. **4**(1): p. 015038.
42. Zhang, L.B., et al., Electrical switching of the edge channel transport in HgTe quantum wells with an inverted band structure. Physical Review B, 2011. **83**(8).
43. Knight, P.L. and P.W. Milonni, The Rabi frequency in optical spectra. Physics Reports, 1980. **66**(2): p. 21-107.
44. Hendrickx, N.W., et al., A four-qubit germanium quantum processor. Nature, 2021. **591**(7851): p. 580-585.

45. Lawrie, W.I.L., et al., Spin relaxation benchmarks and individual qubit addressability for holes in quantum dots. Nano letters, 2020. **20**(10): p. 7237-7242.
46. Kibis, O., et al., Matter coupling to strong electromagnetic fields in two-level quantum systems with broken inversion symmetry. Physical review letters, 2009. **102**(2): p. 023601.
47. Ominato, Y., J. Fujimoto, and M. Matsuo, Valley-dependent spin transport in monolayer transition-metal dichalcogenides. Physical Review Letters, 2020. **124**(16): p. 166803.
48. White, R. and D. Friedman, Theory of the magnetic proximity effect. Journal of magnetism and magnetic materials, 1985. **49**(1-2): p. 117-123.
49. Echeverry, J., et al., Splitting between bright and dark excitons in transition metal dichalcogenide monolayers. Physical Review B, 2016. **93**(12): p. 121107.
50. Yan, X., et al., High performance piezotronic spin transistors using molybdenum disulfide nanoribbon. Nano Energy, 2020. **75**: p. 104953.
51. Lond, R.S., [2] JD Jackson, Classical electrodynamics, (John Wiley & Sons, Hoboken, NJ, 1999). Opt. Express, 2007. **15**: p. 6431.
52. Yoshihara, F., et al., Flux qubit noise spectroscopy using Rabi oscillations under strong driving conditions. Physical Review B, 2014. **89**(2): p. 020503.
53. Garcia-Pomar, J., A. Cortijo, and M. Nieto-Vesperinas, Fully valley-polarized electron beams in graphene. Physical review letters, 2008. **100**(23): p. 236801.
54. Schoenfield, J.S., B.M. Freeman, and H. Jiang, Coherent manipulation of valley states at multiple charge configurations of a silicon quantum dot device. Nature communications, 2017. **8**(1): p. 64.
55. Takeda, K., et al., A fault-tolerant addressable spin qubit in a natural silicon quantum dot. Science advances, 2016. **2**(8): p. e1600694.
56. Maugin, G.A., Continuum mechanics of electromagnetic solids. 2013: Elsevier.
57. Hu, G., et al., Piezotronic Transistor Based on Topological Insulators. ACS Nano, 2018. **12**(1): p. 779-785.
58. Kamberaj, H., Electromagnetic Waves in Dispersive Media, in Electromagnetism: With Solved Problems. 2022, Springer. p. 359-378.
59. Song, K., et al., Correlative high-resolution mapping of strain and charge density in a strained piezoelectric multilayer. Advanced Materials Interfaces, 2015. **2**(1): p. 1400281.
60. Zhang, C., et al., Strain distributions and their influence on electronic structures of WSe2–MoS2 laterally strained heterojunctions. Nature nanotechnology, 2018. **13**(2): p. 152-158.
61. Song, Y. and H. Dery, Transport theory of monolayer transition-metal dichalcogenides through symmetry. Physical review letters, 2013. **111**(2): p. 026601.
62. Liu, G.-B., et al., Three-band tight-binding model for monolayers of group-VIB transition metal dichalcogenides. Physical Review B, 2013. **88**(8): p. 085433.
63. Ge, Z., et al., Control of giant topological magnetic moment and valley splitting in trilayer graphene. Physical Review Letters, 2021. **127**(13): p. 136402.
64. Zhao, C., et al., Enhanced valley splitting in monolayer WSe2 due to magnetic exchange field. Nature nanotechnology, 2017. **12**(8): p. 757-762.
65. Qiao, Z., et al., Quantum anomalous Hall effect in graphene proximity coupled to an antiferromagnetic insulator. Physical review letters, 2014. **112**(11): p. 116404.
66. Sie, E.J., et al., Valley-selective optical Stark effect in monolayer WS2. Nature Materials, 2015. **14**(3): p. 290-294.
67. McIver, J.W., et al., Light-induced anomalous Hall effect in graphene. Nature physics, 2020. **16**(1):

p. 38-41.
68. Pisoni, R., et al., Interactions and magnetotransport through spin-valley coupled Landau levels in monolayer MoS 2. Physical review letters, 2018. **121**(24): p. 247701.
69. Scharf, B., et al., Magnetic proximity effects in transition-metal dichalcogenides: converting excitons. Physical review letters, 2017. **119**(12): p. 127403.
70. Rycerz, A., J. Tworzydło, and C. Beenakker, Valley filter and valley valve in graphene. Nature Physics, 2007. **3**(3): p. 172-175.
71. Moghaddam, A.G. and M. Zareyan, Graphene-based electronic spin lenses. Physical review letters, 2010. **105**(14): p. 146803.
72. Groth, C.W., et al., Kwant: a software package for quantum transport. New Journal of Physics, 2014. **16**(6): p. 063065.
73. Baumgartner, C., et al., Supercurrent rectification and magnetochiral effects in symmetric Josephson junctions. Nature nanotechnology, 2022. **17**(1): p. 39-44.
74. Park, D. and N. Kim, Spin and valley polarization of an MoS 2 zigzag nanoribbon with a magnetic barrier via Fano resonance. Physical Review B, 2022. **106**(23): p. 235123.
75. Vila, M., et al., Nonlocal spin dynamics in the crossover from diffusive to ballistic transport. Physical review letters, 2020. **124**(19): p. 196602.
76. Roch, J.G., et al., Spin-polarized electrons in monolayer MoS2. Nature nanotechnology, 2019. **14**(5): p. 432-436.
77. Newman, D. and E. Siegel, Superposition model analysis of Fe3+ and Mn2+ spin-Hamiltonian parameters. Journal of Physics C: Solid State Physics, 1976. **9**(23): p. 4285.
78. Voon, L.C.L.Y. and M. Willatzen, The kp method: electronic properties of semiconductors. 2009: Springer Science & Business Media.
79. Goringe, C., D. Bowler, and E. Hernandez, Tight-binding modelling of materials. Reports on Progress in Physics, 1997. **60**(12): p. 1447.
80. Andersen, O.K. and O. Jepsen, Explicit, first-principles tight-binding theory. Physical Review Letters, 1984. **53**(27): p. 2571.
81. Trauzettel, B., et al., Spin qubits in graphene quantum dots. Nature Physics, 2007. **3**(3): p. 192-196.
82. Huang, W., et al., Electrically driven spin qubit based on valley mixing. Physical Review B, 2017. **95**(7): p. 075403.
83. Kormányos, A., et al., Spin-orbit coupling, quantum dots, and qubits in monolayer transition metal dichalcogenides. Physical Review X, 2014. **4**(1): p. 011034.
84. Tabert, C.J. and E.J. Nicol, Valley-spin polarization in the magneto-optical response of silicene and other similar 2D crystals. Physical Review Letters, 2013. **110**(19): p. 197402.
85. Norden, T., et al., Giant valley splitting in monolayer WS2 by magnetic proximity effect. Nature communications, 2019. **10**(1): p. 4163.
86. Hajati, Y., M. Alipourzadeh, and I. Makhfudz, Spin-and valley-polarized transport and magnetoresistance in asymmetric ferromagnetic WSe 2 tunnel junctions. Physical Review B, 2021. **103**(24): p. 245435.
87. Young, A.F., et al., Spin and valley quantum Hall ferromagnetism in graphene. Nature Physics, 2012. **8**(7): p. 550-556.
88. Zhu, D., et al., Coherent phonon Rabi oscillations with a high-frequency carbon nanotube phonon cavity. Nano Letters, 2017. **17**(2): p. 915-921.
89. Park, H.C., J. Han, and N. Myoung, A strain-engineered graphene qubit in a nanobubble. Quantum

Science and Technology, 2023. **8**(2): p. 025012.
90. Tong, C., et al., Tunable valley splitting and bipolar operation in graphene quantum dots. Nano Letters, 2021. **21**(2): p. 1068-1073.
91. Tong, C., et al., Pauli Blockade of Tunable Two-Electron Spin and Valley States in Graphene Quantum Dots. Physical Review Letters, 2022. **128**(6): p. 067702.
92. Freitag, N.M., et al., Large tunable valley splitting in edge-free graphene quantum dots on boron nitride. Nature nanotechnology, 2018. **13**(5): p. 392-397.
93. Yang, L., et al., Long-lived nanosecond spin relaxation and spin coherence of electrons in monolayer MoS2 and WS2. Nature Physics, 2015. **11**(10): p. 830-834.
94. Liu, X. and M.C. Hersam, 2D materials for quantum information science. Nature Reviews Materials, 2019. **4**(10): p. 669-684.
95. Ye, Z., et al., Probing excitonic dark states in single-layer tungsten disulphide. Nature, 2014. **513**(7517): p. 214-218.
96. Széchenyi, G., L. Chirolli, and A. Pályi, Impurity-assisted electric control of spin-valley qubits in monolayer MoS2. 2D Materials, 2018. **5**(3): p. 035004.
97. Blais, A., et al., Cavity quantum electrodynamics for superconducting electrical circuits: An architecture for quantum computation. Physical Review A, 2004. **69**(6): p. 062320.
98. Brooks, M. and G. Burkard, Electric dipole spin resonance of two-dimensional semiconductor spin qubits. Physical Review B, 2020. **101**(3): p. 035204.
99. Cunningham, P.D., et al., Resonant optical Stark effect in monolayer WS2. Nature communications, 2019. **10**(1): p. 5539.
100. Li, Y.-M., et al., Light-induced exciton spin Hall effect in van der Waals heterostructures. Physical review letters, 2015. **115**(16): p. 166804.
101. Vool, U., et al., Imaging phonon-mediated hydrodynamic flow in WTe2 with cryogenic quantum magnetometry. arXiv preprint arXiv:2009.04477, 2020.
102. Yuan, J., et al., Squeezed metallic droplet with tunable Kubo gap and charge injection in transition metal dichalcogenides. Proceedings of the National Academy of Sciences, 2020. **117**(12): p. 6362-6369.
103. Lu, P., et al., Strain-dependent electronic and magnetic properties of MoS 2 monolayer, bilayer, nanoribbons and nanotubes. Physical Chemistry Chemical Physics, 2012. **14**(37): p. 13035-13040.
104. Maniadaki, A.E., G. Kopidakis, and I.N. Remediakis, Strain engineering of electronic properties of transition metal dichalcogenide monolayers. Solid State Communications, 2016. **227**: p. 33-39.
105. Duerloo, K.-A.N., M.T. Ong, and E.J. Reed, Intrinsic piezoelectricity in two-dimensional materials. The Journal of Physical Chemistry Letters, 2012. **3**(19): p. 2871-2876.

Table 1. Piezopotential and piezoelectric field of TMDs under strain of 3%.

	MoS_2	$MoSe_2$	$MoTe_2$	WS_2	WSe_2	WTe_2
U_{piezo} (V)	0.148	0.139	0.148	0.116	0.112	0.1
E_{piezo} (MV/cm)	1.078	1.012	1.078	0.842	0.816	0.749

Table 2. The Fermi velocity v, the band gap Δ, the coupling constant λ_v and λ_c, the relative dielectric constant ε_r, the piezoelectric coefficients e_{11} of TMDs.

	MoS_2	$MoSe_2$	$MoTe_2$	WS_2	WSe_2	WTe_2	Ref
v (eV*Å)	2.76	2.53	2.33	3.34	3.17	3.04	[23]
Δ (eV)	1.665	1.425	1.05	1.765	1.485	0.995	[23]
λ_v (eV)	0.075	0.095	0.11	0.215	0.235	0.245	[23]
λ_c (eV)	0.008	0.018	0.029	0.001	0.001	-	[23]
ε_r	6.1	7.0	9.1	5.3	6.0	8.2	[104]
e_{11} (C/m)	3.64	3.92	5.43	2.47	2.71	3.6	[105]

Table 3. Rabi frequency of 2D TMDs

	Rabi frequency (MHz)	Ref
MoS_2	250	[98]
$MoSe_2$	229	[100]
WS_2	750	[99]
WSe_2	229	[100]
WTe_2	33	[101]
This work	4200	

Figure caption

Fig. 1. (a) Schematic diagrams of NFN structure based on ML MoS_2. The current direction is along the x-axis. (b) Corresponding schematic diagram of positive and negative charges symmetric centers of MoS_2 controlled by strain. (c) Piezopotential (the red dashed line) and piezoelectric field (the blue solid line) in NFN structure based on ML MoS_2 under tensile strain of 3%, the piezoelectric field is along the x-axis, where L=20 nm is the width of the ferromagnetic region.

Fig. 2. Schematic of band structures of ML MoS_2 in the normal region (the first line) and ferromagnetic region (the second line). The solid lines represent the K valley, the dashed lines represent the K' valley, the red lines represent spin up and the blue lines represent the spin down. (a) and (d) strain=0, without the influence of the piezoelectric field and deformation potential. (b) and (e) strain=3%, the effect of piezoelectric field is considered. (c) and (f) strain=3%, the effect of deformation potential is considered.

Fig. 3. Density distribution of the electron of NFN structure based on ML MoS_2 with Fermi level fixed at -1.05 eV. (a) Density distribution of the up-spin electron in K valley with 0.5% compressive strain. (b) Density distribution of the up-spin electron in K' valley with 0.2% compressive strain.

Fig. 4. The conductance distribution of ML MoS_2 as a function of Fermi level and strain. The effect of piezoelectric field is considered, for (a) K↑, (b) K↓, (c) K′↑, (d) K′↓. The effect of deformation potential is considered, for (e) K↑, (f) K↓, (g) K′↑, (h) K′↓. The effects of piezoelectric field and deformation potential are considered, for (i) K↑, (j) K↓, (k) K′↑, (l) K′↓.

Fig. 5. Spin-polarized ratio P_s of ML TMDs based on the NFN structure, where "1" represents 100% spin up polarization and "-1" stands for 100% spin down polarization, for (a) MoS_2, (b) $MoSe_2$, (c) $MoTe_2$, (d) WS_2, (e) WSe_2, (f) WTe_2.

Fig. 6. Valley-polarized ratio P_v of ML TMDs based on the NFN structure, where "1" represents full K valley polarization and "-1" stands for full K' valley polarization, for (a) MoS_2, (b) $MoSe_2$, (c) $MoTe_2$, (d) WS_2, (e) WSe_2, (f) WTe_2.

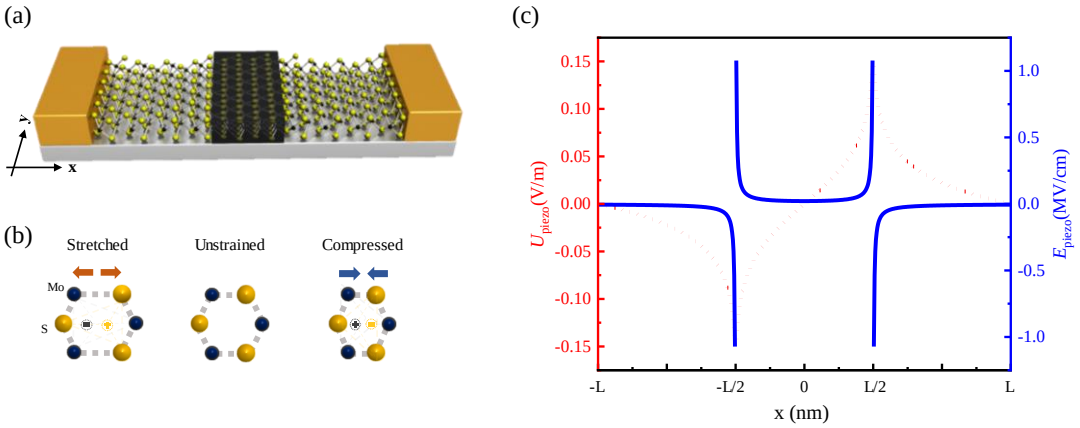
(a)
y
x
(b)
Stretched
Unstrained
Compressed
Mo
S
(c)
0.15
0.10
0.05
0.00
-0.05
-0.10
-0.15
U_{piezo}(V/m)
1.0
0.5
0.0
-0.5
-1.0
E_{piezo}(MV/cm)
-L
-L/2
0
L/2
L
x (nm)

Figure 1

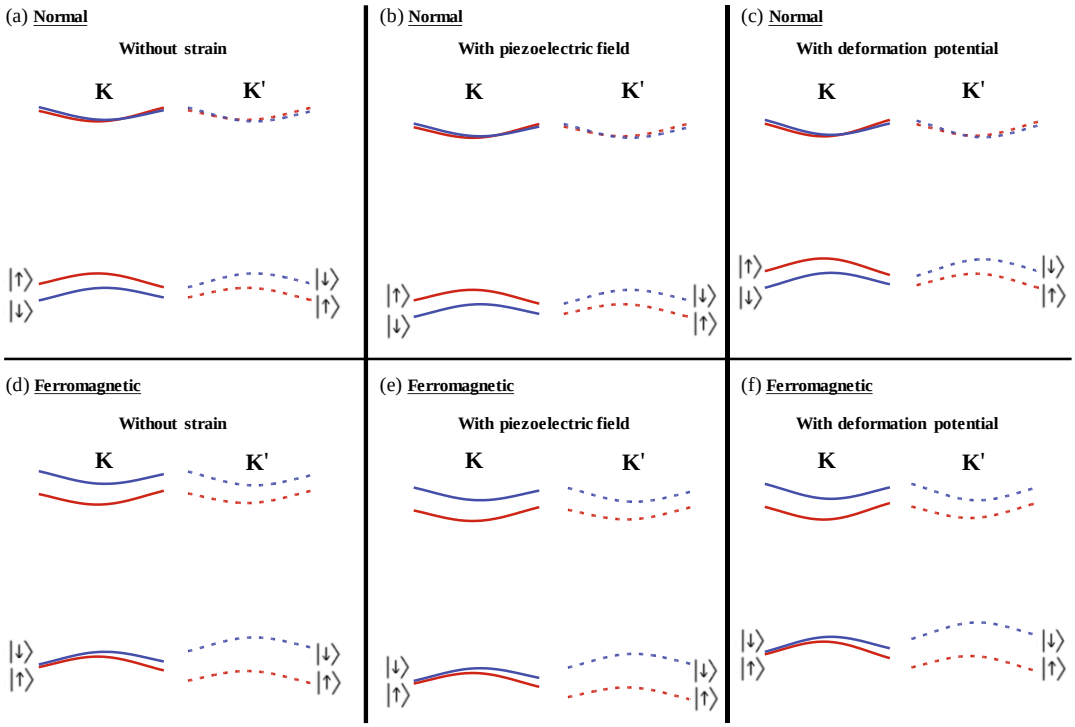
(a) Normal
Without strain
K
K'
|↑⟩
|↓⟩
|↓⟩
|↑⟩
(b) Normal
With piezoelectric field
K
K'
|↑⟩
|↓⟩
|↓⟩
|↑⟩
(c) Normal
With deformation potential
K
K'
|↑⟩
|↓⟩
|↓⟩
|↑⟩
(d) Ferromagnetic
Without strain
K
K'
|↓⟩
|↑⟩
|↓⟩
|↑⟩
(e) Ferromagnetic
With piezoelectric field
K
K'
|↓⟩
|↑⟩
|↓⟩
|↑⟩
(f) Ferromagnetic
With deformation potential
K
K'
|↓⟩
|↑⟩
|↓⟩
|↑⟩

Figure 2

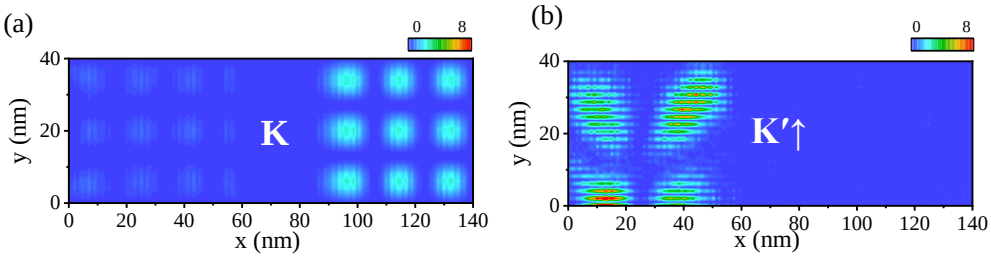
(a)
0
8
40
20
0
y (nm)
K
0
20
40
60
80
100
120
140
x (nm)
(b)
0
8
40
20
0
y (nm)
K′↑
0
20
40
60
80
100
120
140
x (nm)

Figure 3

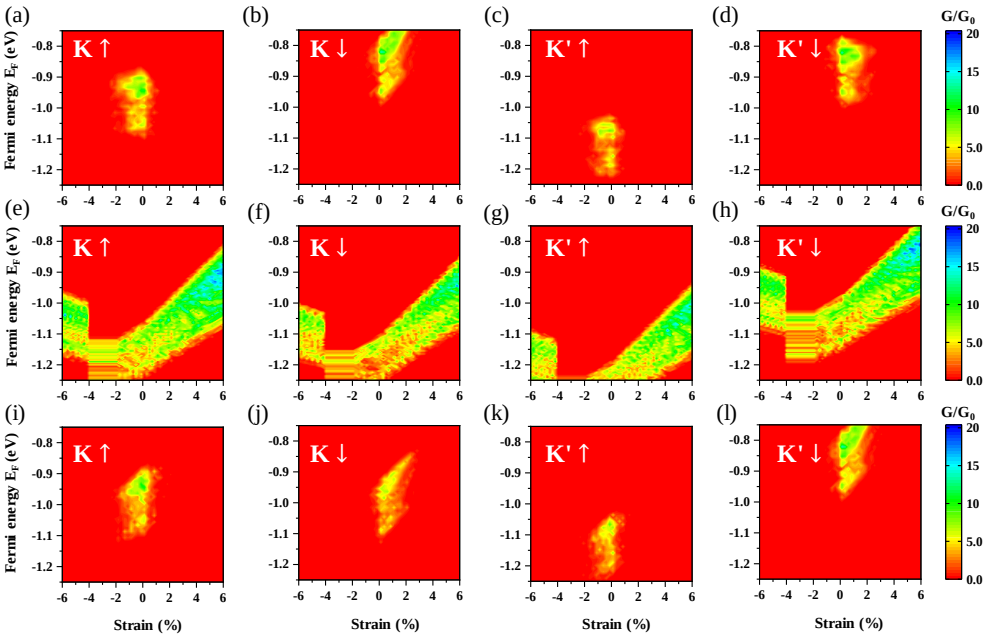

Figure 4

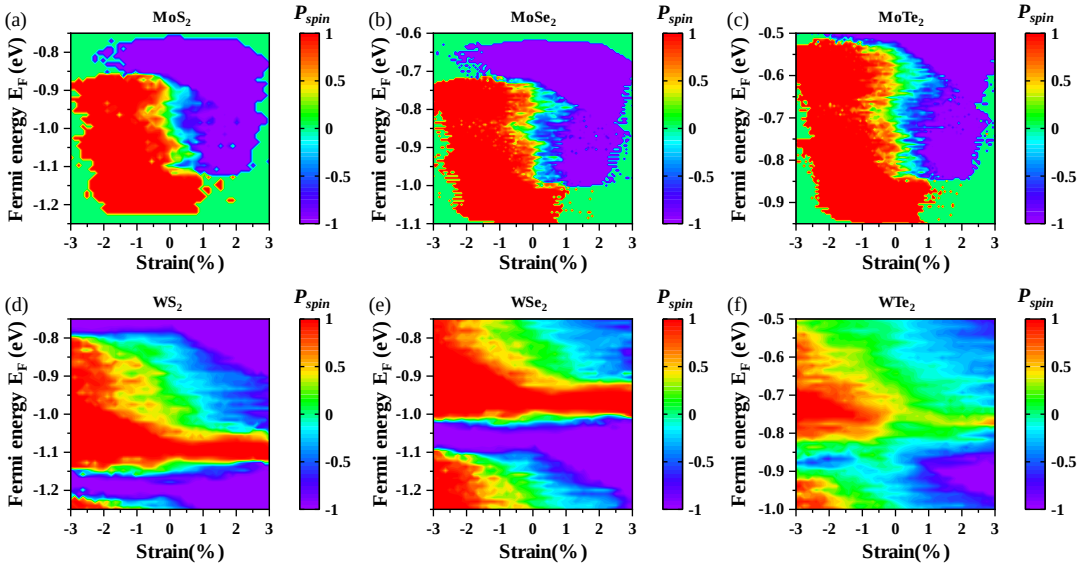
(a)
MoS2
(b)
MoSe2
(c)
MoTe2
(d)
WS2
(e)
WSe2
(f)
WTe2
Pspin
Fermi energy EF (eV)
Strain(%)

Figure 5

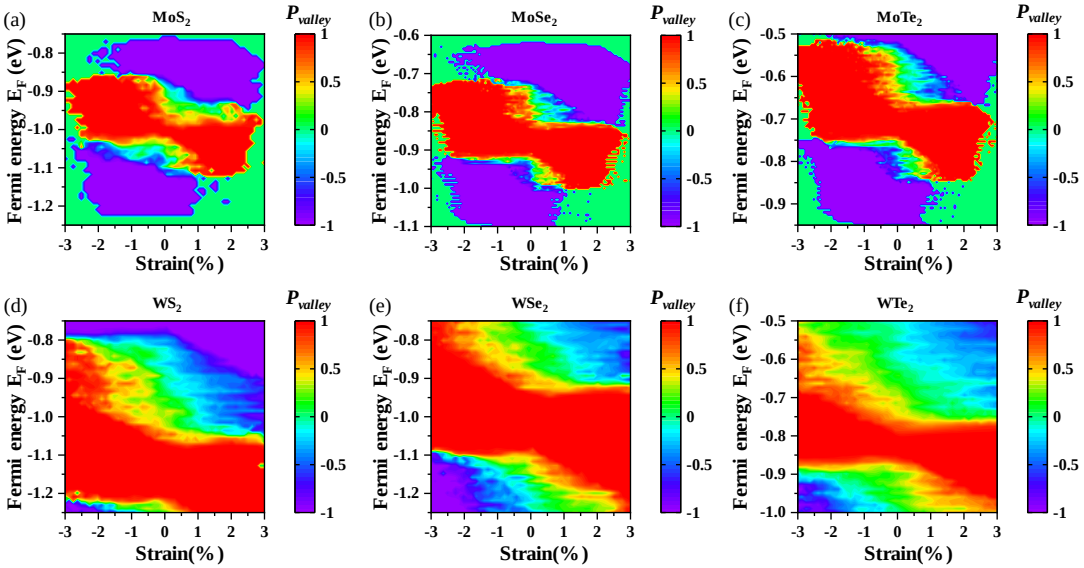
(a)
MoS2
(b)
MoSe2
(c)
MoTe2
(d)
WS2
(e)
WSe2
(f)
WTe2
Pvalley
Fermi energy EF (eV)
Strain(%)

Figure 6